Degradation Mechanisms of Oxygen Evolution Reaction Electrocatalysts: A Combined Identical-Location Transmission Electron Microscopy and X-ray Photoelectron Spectroscopy Study

F. Claudel, Laetitia Dubau, G. Berthome, Lluís Solà-Hernández, Christian Beauger, L. Piccolo, Frédéric Maillard

Degradation Mechanisms of Oxygen Evolution Reaction Electrocatalysts: A Combined Identical-Location Transmission Electron Microscopy and X-Ray Photoelectron Spectroscopy Study

Fabien Claudel,[*,†] *Laetitia Dubau,*[†] *Grégory Berthomé,*[‡] *Lluis Sola-Hernandez,*[§]

Christian Beauger,[§] *Laurent Piccolo,*[∥] *Frédéric Maillard*[*,†]

† Univ. Grenoble Alpes, Univ. Savoie Mont Blanc, CNRS, Grenoble INP, LEPMI, 38000 Grenoble, France

‡ Univ. Grenoble Alpes, CNRS, Grenoble INP, SIMAP, 38000 Grenoble, France

§ MINES ParisTech, PSL University, Centre procédés, énergies renouvelables et systèmes énergétiques (PERSEE), CS 10207 rue Claude Daunesse, F-06904 Sophia Antipolis Cedex, France

‖ Univ Lyon, Université Claude Bernard - Lyon 1, CNRS, IRCELYON - UMR 5256, 2 Avenue Albert Einstein, F-69626 Villeurbanne CEDEX, France

ABSTRACT

Determining the degradation mechanism of oxygen evolution reaction (OER) catalysts is fundamental to design improved polymer electrolyte membrane water electrolyser (PEMWE) devices but remains challenging under the demanding conditions of PEMWE anodes. To address this issue, we introduce a methodology combining identical-location transmission electron microscopy, X-ray photoelectron spectroscopy and electrochemical measurements, and apply it to iridium nanoparticles (NPs) covered by a thin oxide layer (IrO_x) in OER conditions. The results show that, whatever the initial OER activity of the IrO_x nanocatalysts, it gradually declines and reaches similar values after 30,000 potential cycles between 1.20 and 1.60 V *vs*. RHE. This drop in OER activity was bridged to the progressive increase of the Ir oxidation state (fast change during electrochemical conditioning, milder changes during accelerated stress testing) along with increased

concentration of hydroxyl groups and water molecules. In contrast, no change in the mean oxidation state, no change in the hydroxyl/water coverage and constant OER activity were noticed on the benchmark micrometre-sized IrO_2 particles. Besides chemical changes, Ir dissolution/redeposition and IrO_x nanoparticle migration/agglomeration/detachment were evidenced in OER conditions. By combining the information derived from identical-location transmission electron microscopy (IL-TEM) images and X-ray photoelectron spectroscopy (XPS) measurements, we show that Ir(III) and Ir(V) are the best performing Ir valencies for the OER. These findings provide insights into the long-term OER activity of IrO_x nanocatalysts, as well as practical guidelines for the development of more active and more stable PEMWE anodes.

KEYWORDS: Proton-exchange membrane water electrolysers; oxygen evolution reaction; iridium oxide; antimony-doped tin oxide; identical-location transmission electron microscopy.

INTRODUCTION

During the 21st Conference of the Parties held in Paris in 2015, 195 states have agreed to limit global warming to an average of no more than 2 °C relative to pre-industrial level. However, this ambitious objective will not be reached without integrating non-hydro renewables in the energy mix[1]. Additionally, the intermittency of alternative energies calls for a joint development of energy storage systems such as water electrolyzers[2-3]. Of the three main water electrolysis technologies (alkaline, proton exchange membrane (PEM) and solid oxide), PEM water electrolysers (PEMWEs) feature several advantages: they are compact, withstand dynamic operating conditions, and can operate under pressure and at high current densities. However, the massive production of PEMWEs requires (i) enhancing the rate of the oxygen evolution reaction (OER), (ii) improving the durability of the anodic catalytic material, and (iii) decreasing the cost of the catalytic layers *e.g.* by reducing the noble metal content.

Experimental work performed more than 40 years ago has established that ruthenium oxide (RuO_2) is the most efficient catalyst towards the OER in alkaline media but this oxide is unstable in acidic media[4-9]. Iridium oxide (IrO_2) is also highly active for the OER, chemically stable, a good electronic conductor but suffers of its high cost and scarcity especially when used in the form of micrometer-sized particles as it is in state-of-the-art PEMWE anodes[5-8, 10-16]. Solutions to diminish the iridium (Ir) content have been intensively investigated, for example partial substitution of Ir by a transition metal[11-12, 17-22] and/or decrease of the size of the Ir crystallites to the nanometer scale[23-24]. However, the very oxidizing environment of PEMWE anodes (electrochemical potential $E > 2.0$ V *vs*. the reversible hydrogen electrode - RHE, presence of oxygen, highly acidic environment) renders classical high surface area carbon supports unstable[25] and requires the development of alternatives such as metal oxides [26-29]. In addition, it is well-established that the chemical nature and the crystallographic structure of the IrO_x are keys to high and sustainable OER activity; in particular thermal oxides are known to be less active but more stable than electrochemically formed oxides[30-35]. However, because the energy of the metal-oxygen bonds is stronger than that of the oxygen-oxygen bonds,[6]

metal-oxygen bonds are permanently formed and broken in OER conditions. Thus, the chemical composition and the intrinsic activity of OER catalysts continuously change in PEMWE anode operating conditions more specifically at the nanometre-scale[33, 36-37].

Surprisingly, despite its great fundamental and technological interest, the fate of supported-IrO_x nanocatalysts in OER conditions has never been studied hitherto. To adresss this issue, we introduce for the first time a methodology combining identical-location transmission electron microscopy (IL-TEM), X-ray photoelectron spectroscopy (XPS) and electrochemical measurements, and apply it to iridium nanoparticles (NPs) covered by a thin oxide layer.

RESULTS AND DISCUSSION

Initial Morphology, Structure and Chemical Composition of Antimony-doped Tin Oxide-supported and Carbon-supported IrO_x Nanoparticles

Figure 1a-h shows TEM images IrO_x NPs supported on Vulcan XC-72 (IrO_x/C) or on antimony-doped tin oxide aerogel (IrO_x/ATO) synthesized in house using the same colloidal solution, and two commercial catalysts: metallic Ir NPs supported on Vulcan XC-72 (Ir/C comm.) and IrO_2 powder (IrO_2 comm.). In the IrO_x/C catalyst, the metal NPs feature an average diameter of 1.9 ± 0.5 nm and are homogeneously distributed onto the carbon support. The IrO_x/ATO NPs exhibit similar size (2.0 ± 0.5 nm) but are more agglomerated when supported on ATO. Similar observations were made by Cognard *et al.*[38] on Pt/C and Pt/ATO nanocatalysts, and the differences of agglomeration were ascribed to different specific surface areas of the supports. Finally, a mix of large aggregates and small NPs co-exist in the commercial Ir/C and IrO_2 catalysts, thus explaining why the crystallite size of Ir/C exceeds the nanoparticle size.

The X-ray diffraction patterns (**Figure 1i**, **j**) indicate that Ir/C comm. is essentially metallic, and that small amorphous or poorly crystallize) IrO_2 nanocrystallites and large metallic Ir crystallites co-exist in the IrO_2 comm. sample. The presence of broad diffraction peaks for IrO_x/C and IrO_x/ATO suggests small and/or amorphous NPs in these samples.

No reflection typical of tetragonal IrO_2 (PDF card n° 04-009-8479) was detected in the as-synthesized and benchmark materials.

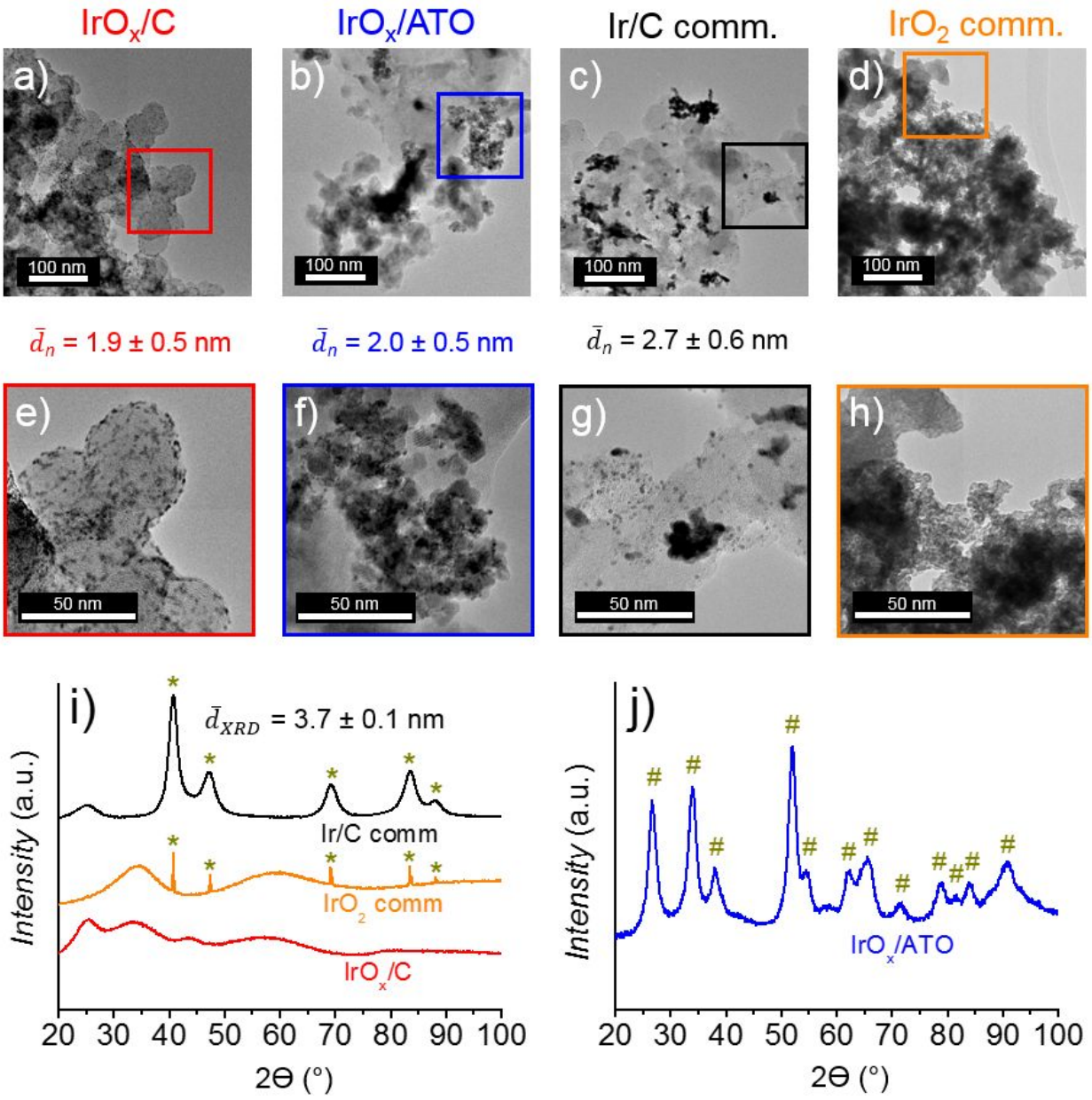

Figure 1. TEM images of IrO_x/C (a, e), IrO_x/ATO (b, f), Ir/C comm. (c, g) and IrO_2 comm. (d, h). X-ray diffractograms of Ir/C comm., IrO_2 comm. and IrO_x/C (i), and IrO_x/ATO (j). The star and the hash symbols correspond to cubic Ir (PDF card n° 00-006-0598) and tetragonal SnO_2 (PDF card n° 00-041-1445), respectively. No reflection typical of tetragonal IrO_2 (PDF card n° 04-009-8479) was detected in the as-synthesized and benchmark materials.

Insights into the chemical nature of the IrO_x surface atoms were obtained by XPS measurements. The Ir4f spectra displayed in **Figure 2** were fitted using the parameters and the line shapes recently provided by Freakley *et al.*[39] (see **Table S1** and Materials and Methods for more details). Four contributions were considered: metallic Ir, Ir(III), Ir(IV) and Ir(V) species. **Figure 2** and **Table S2** indicate that: (i) Ir/C comm. is essentially metallic (**Figure 2c**), (ii) Ir(IV) species predominate in the IrO_x/C (**Figure 2a**) and IrO_2 comm. (**Figure 2d**) catalysts and that (iii) despite the same colloidal solution was used for the

synthesis of IrO_x/C and IrO_x/ATO catalysts, metallic Ir, Ir(III), Ir(IV), and Ir(V) species co-exist in the fresh IrO_x/ATO (**Figure 2b**).

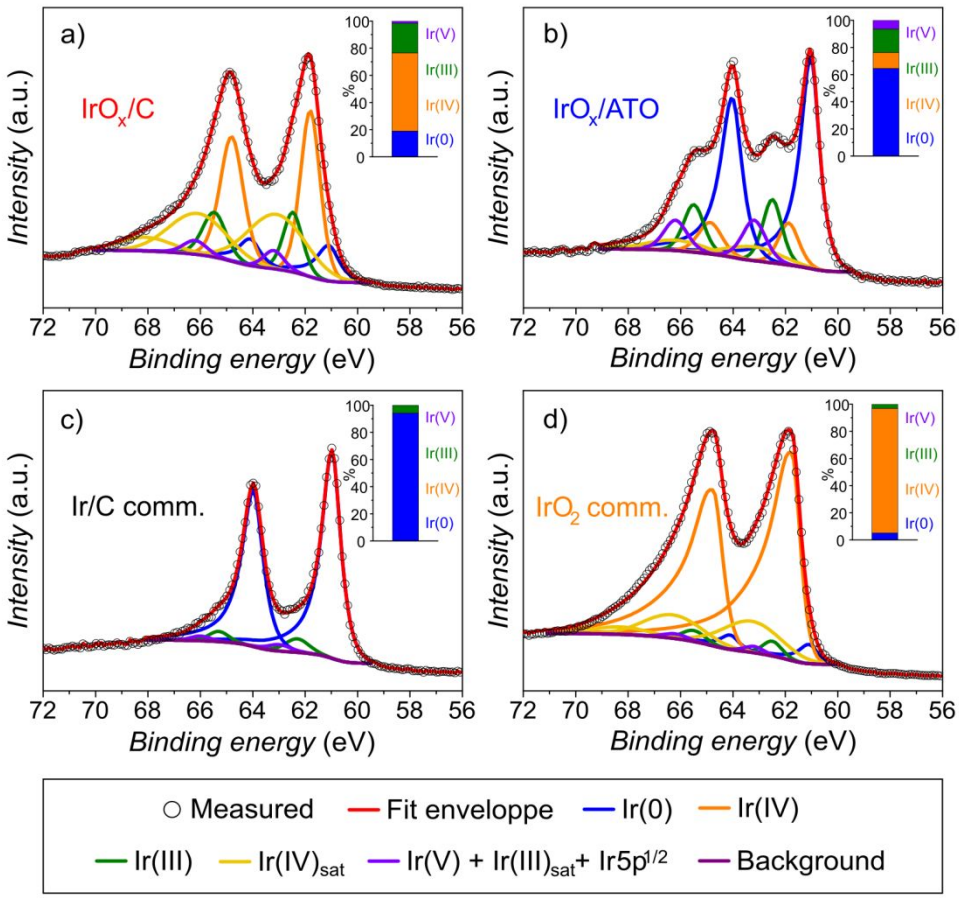

Figure 2. X-ray photoelectron spectra (Ir4f level) for IrO_x/C (a), IrO_x/ATO (b), Ir/C comm. (c) and IrO_2 comm. (d). The Ir(V) content was calculated by subtracting 15% of the area of the peak attributed to Ir(III) and 2.67% of the total area of the Ir4f band (to account for

the theoretical contribution of Ir(III) satellites and $Ir5p_{1/2}$, respectively) to the areas of the peaks located at 63.1 and 66.1 eV.

Electrocatalytic Activity for the Oxygen Evolution Reaction in Acidic Electrolyte

Changes of the cyclic voltammograms (CVs) during 'electrochemical conditioning' (100 potential cycles between 0.05 and 1.40 V *vs.* RHE at 500 mV s^{-1}) confirmed the XPS results. Indeed, the electrical charge associated with the adsorption/desorption of underpotentially-deposited hydrogen (H_{upd}) gradually decreased during the conditioning cycles on Ir/C comm. (**Figure 3a**). In contrast, the CVs stabilized after *ca*. 25 potential cycles for the IrO_x/C catalyst (**Figure 3b**), thus confirming that the IrO_x/C NPs were partly oxidized in the fresh state. An intermediate behaviour was observed for the IrO_x/ATO catalyst (**Figure 3c**): H_{upd} features were observed during the first conditioning cycles but rapidly disappeared highlighting that the NPs were in average more metallic in IrO_x/ATO than in IrO_x/C. Last, the CVs measured on IrO_2 comm. featured no change (**Figure 3d**), in agreement with the predominance of Ir(IV) species in this catalyst.

Ohmic-drop corrected polarization curves in 0.05 M H_2SO_4 (**Figure 4a-c**) were used to determine the OER activities of the different nanocatalysts. We are aware that a fraction of the measured current arises from the electrochemical dissolution of the IrO_x NPs. However, based on dissolution rates of 10 and 0.1 ng cm^{-2} established for metallic Ir and IrO_2 electrodes, respectively [40] we estimated that the Ir dissolution current contributed to less than 0.05 % to the total electrical charge of the OER polarization curve.

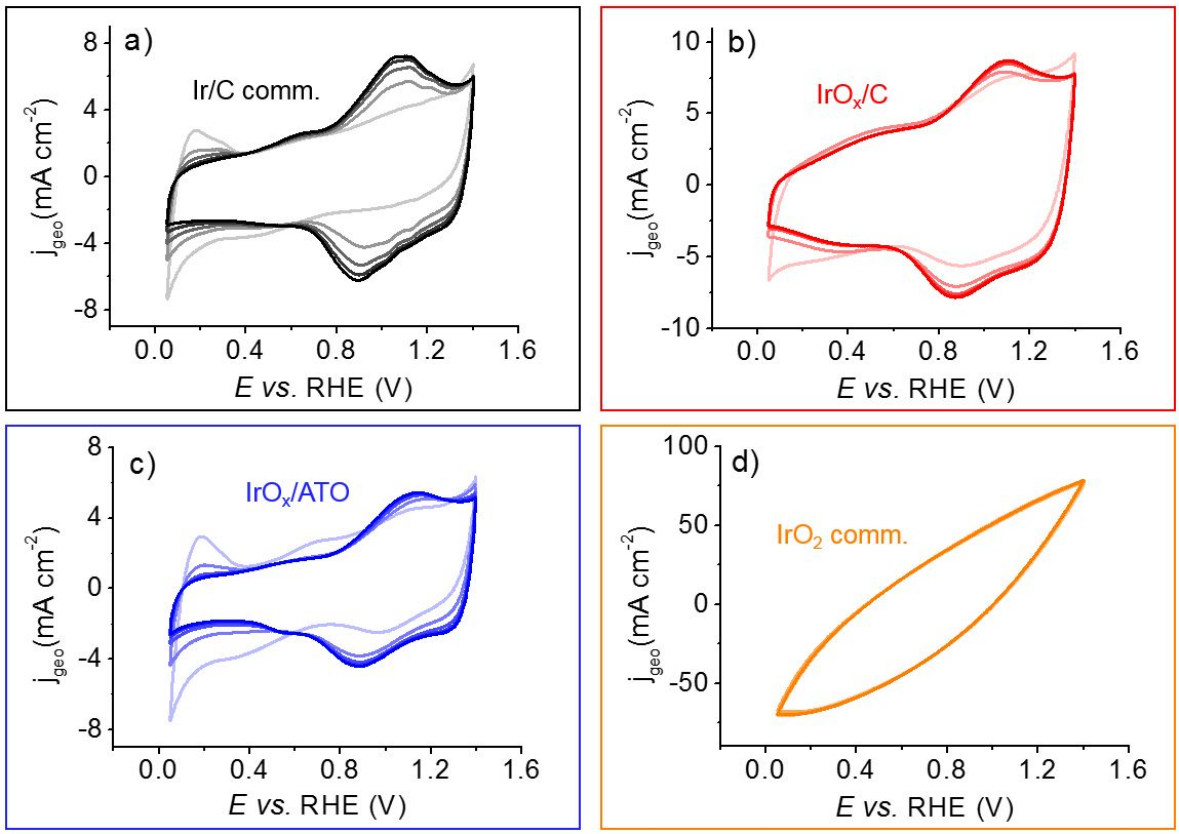

Figure 3. Conditioning cycles between 0.05 and 1.40 V *vs.* RHE in Ar-saturated 0.05 M H_2SO_4 electrolyte on (a) Ir/C comm., (b) IrO_x/C, (c) IrO_x/ATO and (d) IrO_2 comm. The potential sweep rate was 500 mV s^{-1}. The shades of colours (lightest to darkest) represent the 2nd, 25th, 50th, 75th and 100th potential cycles.

The Ohmic-drop corrected OER current measured at 1.51 V *vs.* RHE (η = 280 mV) normalized by the initial mass of Ir on the electrode (j_{mass}) or by the anodic charge obtained after integration of the current between 0.40 and 1.40 V *vs.* RHE (j_{spec}) and the background corrected OER specific activities using IrO_x NPs-free supports ($j_{spec\text{-}support}$) is displayed in **Figure 4d**, **Figure 4e** and **Figure 4f**, respectively. The mass activity towards the OER of all catalysts approached the recent record value of 100 A g_{Ir}^{-1} reported in Ref. [41] and reached an optimal value for IrO_x/C (221 ± 14 A g_{Ir}^{-1}). Using the conclusions derived from XPS spectra (**Table S2**), we can thus confidently confirm that amorphous nanometer-sized Ir oxides containing a mixture of Ir(0), Ir(III) and Ir(IV) species better

perform than crystalline nanometer-sized Ir oxides containing predominantly Ir(IV) species [36].

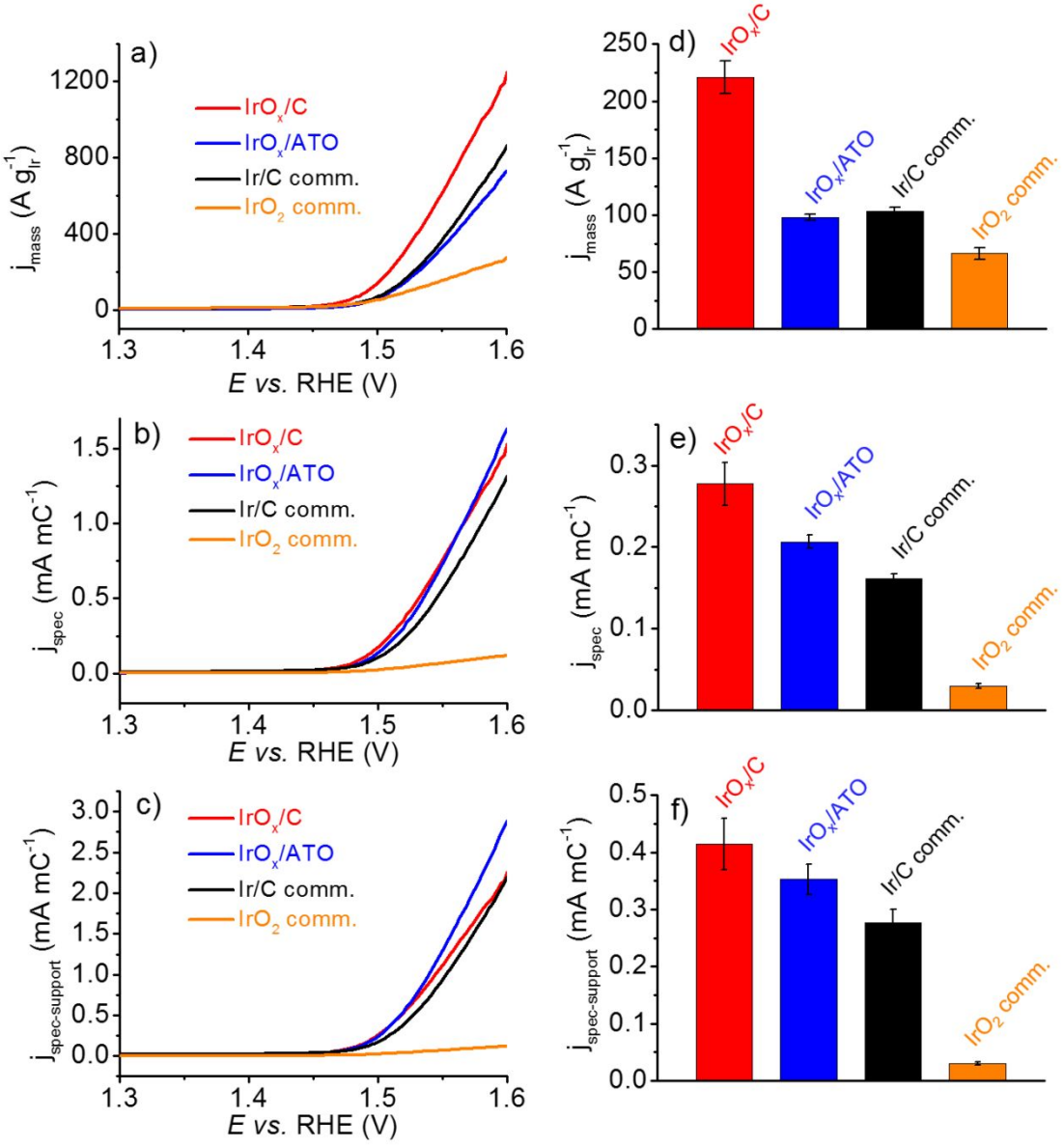

Figure 4. Ohmic-drop corrected polarization curves measured between 1.20 and 1.60 V *vs.* RHE at 5 mV s^{-1} and 293 K in Ar-saturated 0.05 M H_2SO_4. The OER current was

determined at E = 1.51 V vs. RHE, and normalized by (a) the mass of Ir initially loaded onto the electrode (j_{mass}), (b) the anodic charge obtained by integrating the current between 0.40 and 1.40 V *vs.* RHE (j_{spec}), and (c) the anodic charge obtained by integrating the current between 0.40 and 1.40 V *vs.* RHE after background subtraction ($j_{spec\text{-}support}$). The experiments were repeated three times and the error bars correspond to the standard deviation of the measurements.

Changes of the Oxygen Evolution Reaction Activity in OER Conditions

The catalytic powders were then electrochemically aged using an accelerated stress test (AST) comprising 30,000 potential steps between 1.20 and 1.60 V *vs.* RHE with square-wave potential ramp (3 s at each potential). **Figure 5a-d** show the CVs measured on the fresh and aged Ir/C comm., IrO_x/C, IrO_x/ATO and IrO_2 comm. catalysts. For all materials, except IrO_2 comm., the anodic charge between 0.40 and 1.40 V *vs.* RHE increased during the first 1,000 (1 k) potential cycles, more remarkably on IrO_x/C, suggesting continuous growth of an electrochemical oxide layer[17, 42]. Also, a peak

commonly associated to the Ir(III)/Ir(IV) transition[33, 43-44] was noticed at *ca*. 0.97/0.93 V *vs.* RHE (positive-and negative-going potential sweep, respectively) on the three supported catalysts. This peak was broad for the fresh IrO_x/C and IrO_x/ATO but it sharpened and shifted towards negative potentials during the first AST cycles, thus suggesting a change in the nature of the surface species (**Figure 5b** and **Figure 5c**). It was already sharp and negatively shifted for the fresh Ir/C comm. catalyst (**Figure 5a**). Remarkably, another redox peak emerged at 1.20 V *vs.* RHE (positive-going potential sweep) after 10,000 (10 k) potential cycles on IrO_x/C or after 4,000 (4 k) potential cycles on IrO_x/ATO and Ir/C comm. It was formerly documented by Saveleva *et al.*[36] and by Oh *et al.*[24] for Ir@IrO_x catalysts and Ir nanodendrites, respectively. Oh *et al.*[24] ascribed this peak to the transition of Ir(IV) to Ir(V) although this change in Ir oxidation state may occur at *ca*. 1.40-1.45 V *vs.* RHE, as suggested by the redox peaks observed on the CVs in other works [30, 33, 43-44]. An alternative explanation was provided by Pfeifer *et al.* [45]: using density functional theory, these authors proposed that this peak should be rather ascribed to the oxidation of O(-II) in O(-I). They predicted a standard potential approaching 1.20 - 1.30 V *vs*. RHE for this reaction, in excellent agreement with our results.

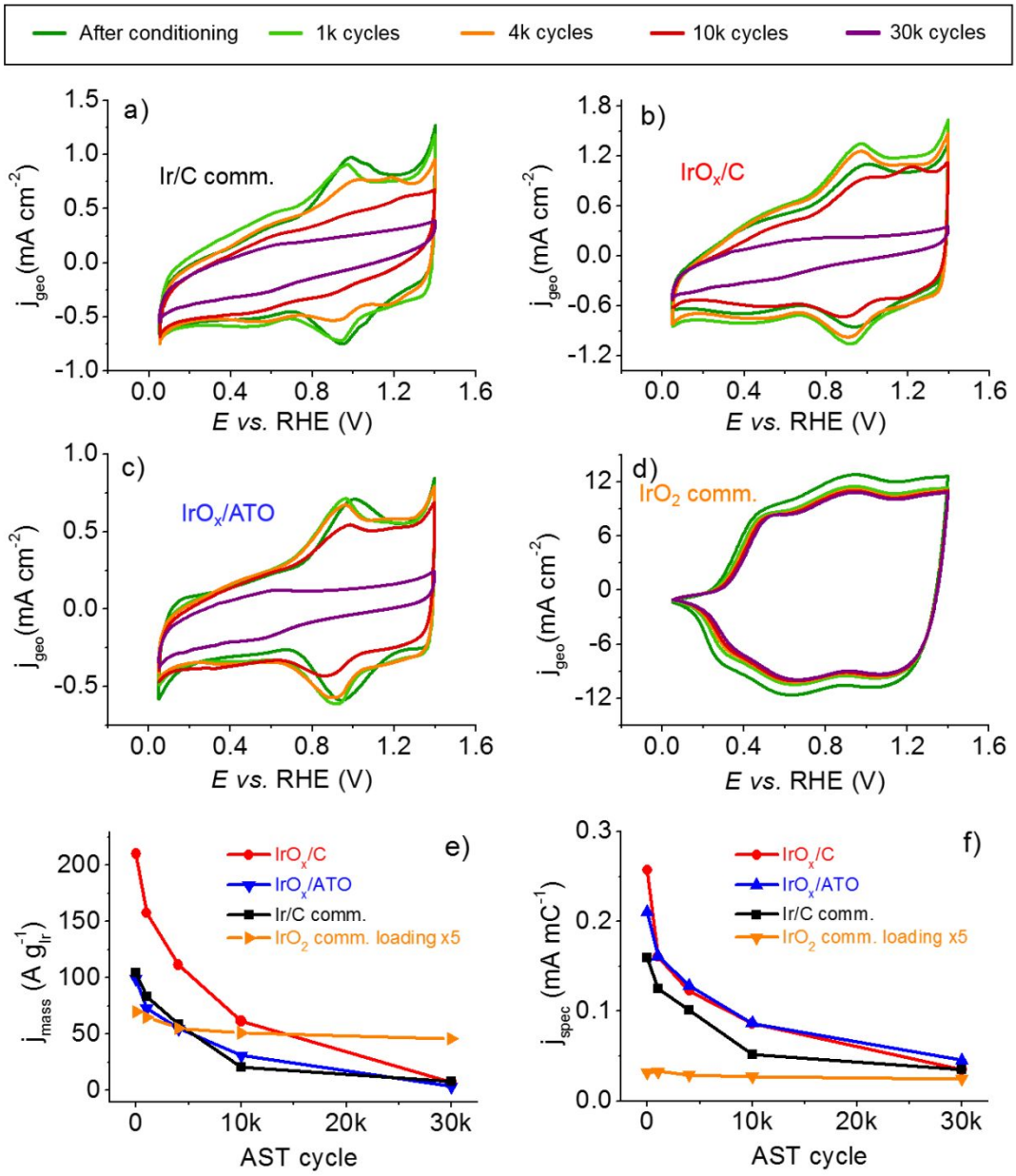

Figure 5. Cyclic voltammograms recorded in Ar-saturated 0.05 M H_2SO_4 at 50 mV s^{-1} at 293 K after the conditioning step (100 cycles between 0.05 and 1.40 V *vs.* RHE) and after 1,000, 4,000, 10,000 and 30,000 potential cycles between 1.20 and 1.60 V *vs.* RHE

for a) Ir/C comm., b) IrO_x/C, c) IrO_x/ATO and d) IrO_2 comm. Changes of the OER catalytic activity measured at 1.51 V *vs.* RHE as a function of the number of cycles for the four catalysts investigated in this study. The OER activity was normalized by e) the mass of Ir initially loaded onto the electrode (j_{mass}) and f) the anodic charge obtained by integrating the current between 0.40 and 1.40 V *vs.* RHE (j_{spec}).

As shown by **Figure 5e** and **Figure 5f**, the OER performance dropped for all supported catalysts during the AST. IrO_x/C remained the most active electrocatalyst both from mass and specific activity perspectives during the first 10 k potential cycles but IrO_2 comm. revealed the most robust catalyst in terms of mass activity towards the OER (**Figure 5e**), the most important metrics in terms of PEMWE device. Fitting the Tafel plots in the linear region of the $\eta = f(\log(j_{mass}))$ plots (**Figure S2**) confirmed the drop in performance during the AST. In the fresh state, Tafel slopes of 52 and 50 mV dec^{-1} were obtained for IrO_x/C and IrO_x/ATO, respectively and higher values were obtained for Ir/C comm. and IrO_2 comm. (58 and 78 mV dec^{-1}, respectively). These values increased on all supported-electrocatalysts after 10 k potential cycles.

Morphological Evolution of the Nanocatalysts during AST Monitored by IL-TEM

To disclose chemical composition-morphology-OER activity relationships, the morphological changes occurring on IrO_x/C, IrO_x/ATO and Ir/C comm. during the AST were assessed using IL-TEM. The IL-TEM images were recorded in the fresh state (as-synthesized), after conditioning, and after 1 k, 4 k, 10 k and 50 k potential cycles. Key to these measurements was to use a TEM grid made of titanium (indeed, gold TEM grids dissolve at potential > 1.40 V *vs*. RHE [46]). To the best of our knowledge, this is the first time that IL-TEM measurements are performed in OER conditions.

The changes in morphology for the three supported nanocatalysts are displayed in **Figure 6**. Quantitative information was derived from the IL-TEM images: the average Feret diameter was measured for the exact same NPs in the fresh state, and after conditioning, 1 k, 4 k, 10 k and 50 k potential cycles. The NP size distributions of the fresh and aged IrO_x/C, IrO_x/ATO and Ir/C comm. catalysts determined by eye-counting using the ImageJ software (automated determination revealed less precise, see **Figure S5**) are

displayed in **Figure 7**, **Figure S3** and **Figure S4**, respectively. They show that the smallest IrO_x/C and IrO_x/ATO NPs preferentially disappeared during the conditioning step along with a small increase in NP size, thus suggesting that Ostwald ripening occurred during this stage. In contrast, during the AST, crystallite migration/agglomeration/coalescence and detachment of the largest IrO_x NPs were the predominant degradation mechanisms. These results are in excellent agreement with the inductively-coupled plasma mass spectrometry results of Cherevko *et al.*[43-44, 47-48] pointing towards dissolution of bulk Ir surfaces in similar potential conditions. They also agree with thermodynamics,[49] as Ir^{3+} ions produced by dissolution can redeposit in the metallic form only onto for potentials below *ca*. 1.16 V *vs*. RHE that is during the conditioning step.

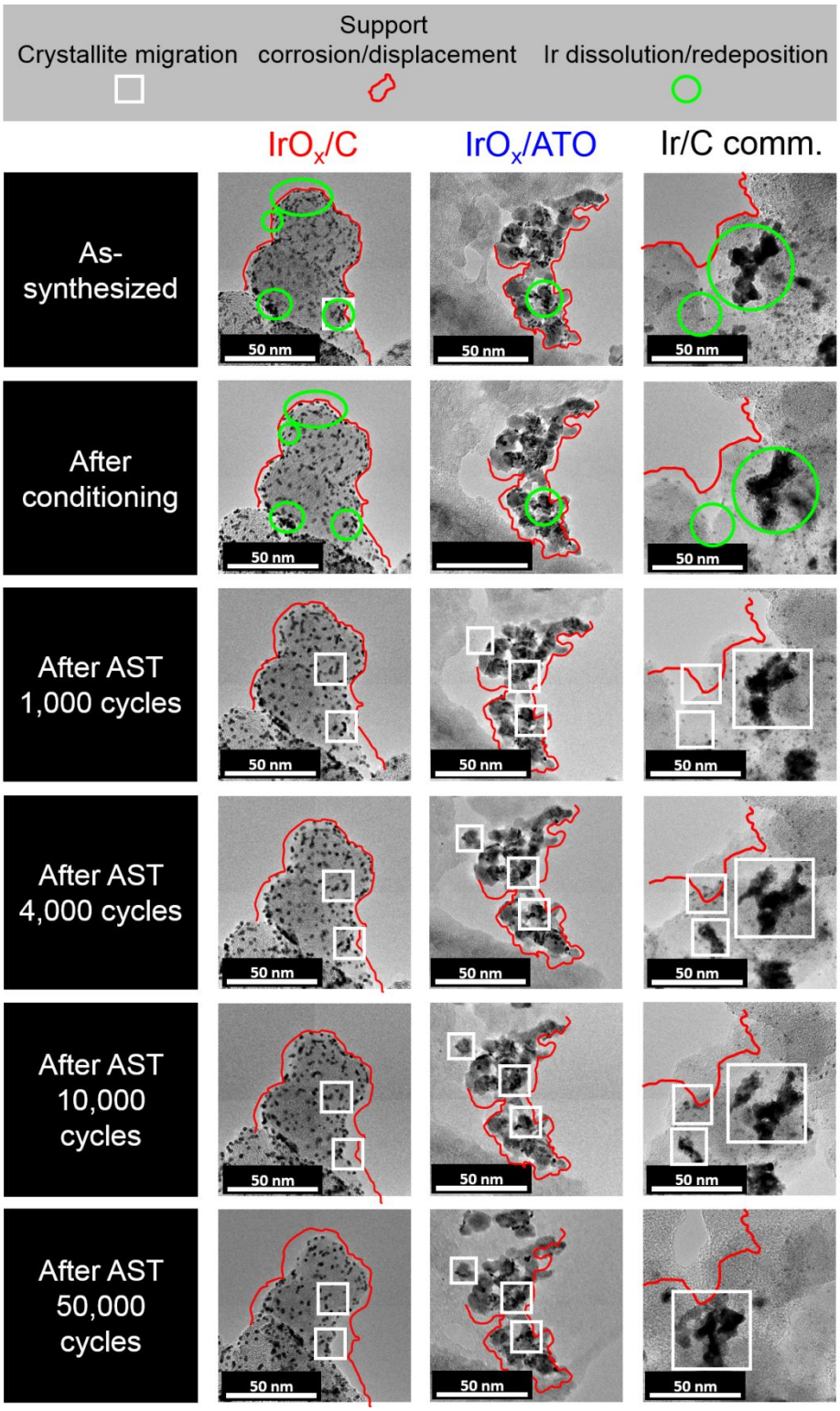
Crystallite migration
Support corrosion/displacement
Ir dissolution/redeposition
IrOx/C
IrOx/ATO
Ir/C comm.
As-synthesized
After conditioning
After AST 1,000 cycles
After AST 4,000 cycles
After AST 10,000 cycles
After AST 50,000 cycles
50 nm

Figure 6. IL-TEM images of IrO_x/C, IrO_x/ATO and Ir/C comm. as-synthesized, after the conditioning step (0.05 < *E* < 1.60 V *vs*. RHE) and after different stages of potential cycling between 1.20 < *E* < 1.60 V *vs*. RHE, highlighting major degradation mechanisms occurring during OER.

Along with Ir dissolution, a strong corrosion of Vulcan XC72 was noticed, in line with thermodynamics[49] and with former results showing massive carbon corrosion at potentials above 1.50 V *vs.* RHE [50-51]. It is noteworthy that the ATO support was also corroded in OER conditions, indicating mild or no positive metal/metal-oxide support interaction effect. This statement was supported by X-EDS measurements showing a gradual loss of Sb atoms from the conditioning stage leading. After 50 k potential cycles, there was no Sb remaining in the ATO aerogel thus attenuating the ability of the IrO_x NPs to exchange electrons. These results are in line with former report by Cognard *et al*. [52] showing dissolution and concomitant restructuration of ATO in PEMFC cathode operating conditions. By combining rotating disk and rotating ring disk electrode, X-ray energy dispersive X-ray spectroscopy and inductively-coupled plasma mass spectrometry, the

authors showed that both Sb and Sn atoms are dissolved from ATO. The concomitant restructuration of the ATO support was accelerated during potential excursions at low electrode potential, *e.g.* during electrochemical characterizations or kinetic measurements.

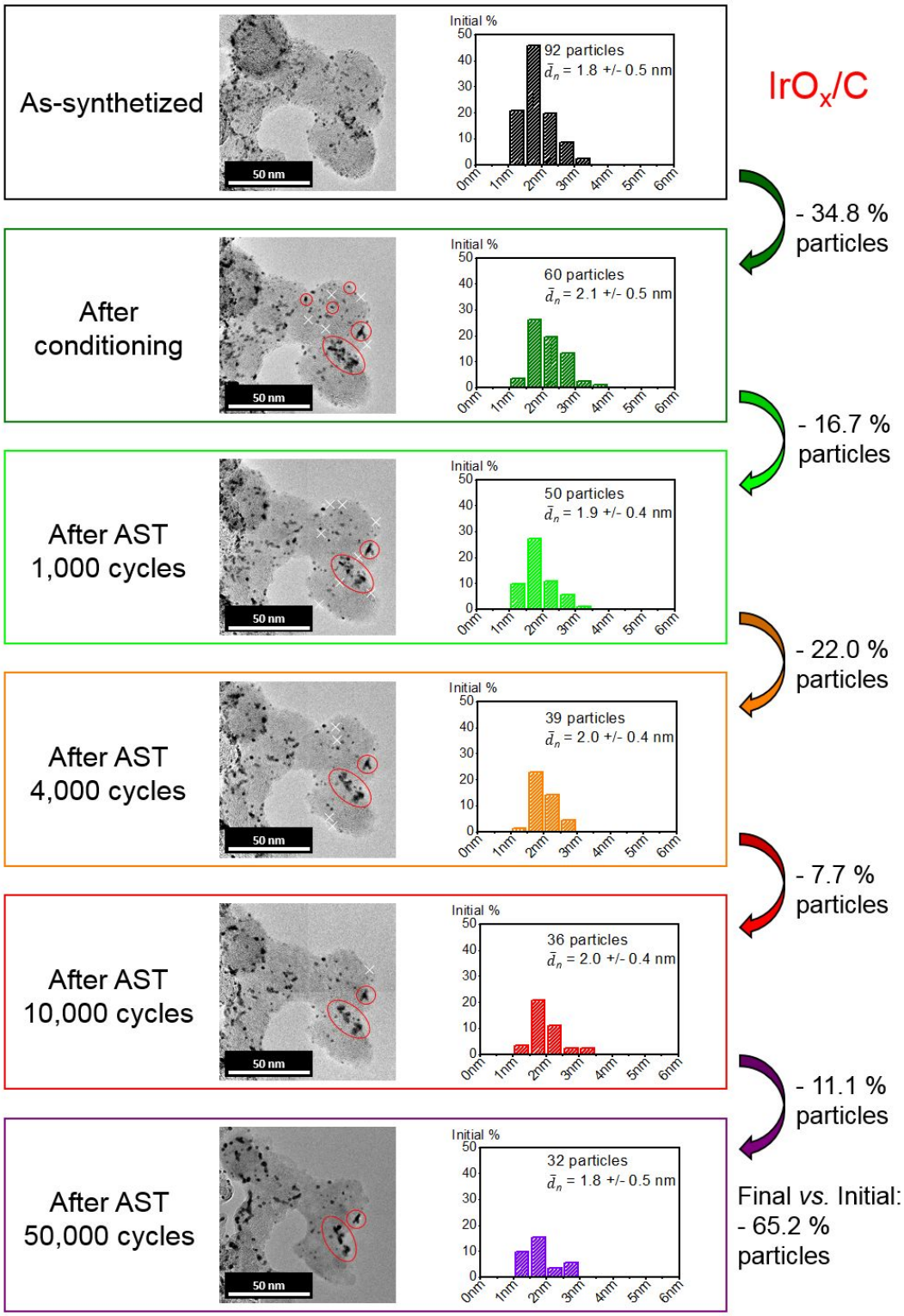
As-synthetized
50 nm
Initial %
92 particles
$\bar{d}_n$ = 1.8 +/- 0.5 nm
IrO_x/C
- 34.8 % particles
After conditioning
50 nm
Initial %
60 particles
$\bar{d}_n$ = 2.1 +/- 0.5 nm
- 16.7 % particles
After AST 1,000 cycles
50 nm
Initial %
50 particles
$\bar{d}_n$ = 1.9 +/- 0.4 nm
- 22.0 % particles
After AST 4,000 cycles
50 nm
Initial %
39 particles
$\bar{d}_n$ = 2.0 +/- 0.4 nm
- 7.7 % particles
After AST 10,000 cycles
50 nm
Initial %
36 particles
$\bar{d}_n$ = 2.0 +/- 0.4 nm
- 11.1 % particles
After AST 50,000 cycles
50 nm
Initial %
32 particles
$\bar{d}_n$ = 1.8 +/- 0.5 nm
Final *vs.* Initial:
- 65.2 % particles
0nm 1nm 2nm 3nm 4nm 5nm 6nm

Figure 7. IL-TEM images and associated changes of the particle size distribution for IrO_x/C during potential cycling between 1.20 < *E* < 1.60 V *vs*. RHE at *T* = 298 K. Only isolated particles were considered to build the histograms. Red ellipses were used to highlight migration/agglomeration/coalescence of IrO_x NPs and white crosses highlight their detachment. The number-averaged average Feret diameter ($\overline{d}_n$) is plotted in the histograms.

Compositional Evolution of the Nanocatalysts During AST Monitored by XPS

Changes in the chemical composition of IrO_x/C, IrO_x/ATO, Ir/C comm. and IrO_2 comm. during the AST were also monitored. As indicated by **Figure 8**, the $Ir4f_{7/2}$ band typically shifted to higher binding energy for all supported catalysts indicating an increase in the oxidation state. This result agrees with the early findings of Kötz *et al*. [33] on anodic Ir oxide films. Similarly, Li *et al*. [53] polarized a 100 nm-thick Ir film at 1 mA cm^{-2} for 4, 69 or 120 hours. Based on XPS measurements, the authors claimed that metastable Ir–O species first form and then transform into IrO_2 in OER conditions. The results displayed in **Figure**

8 confirm these findings but they also indicate that Ir(III), Ir(IV) and Ir(V) species co-exist in the aged nanocatalysts, in agreement with the *operando* XPS results of Sanchez-Casalongue [37]and the X-ray absorption near-edge spectroscopy (XANES) measurements of Minguzzi *et al*. [54-55]. Therefore, the mixture of Ir valencies observed after the AST can be rationalized by considering an Ir cation *red* – *ox* mechanism, such as that recently proposed by Cherevko *et al*.[44]:

$$IrO(OH) \rightarrow IrO_2 + H^+ + e^- \quad (1)$$

$$IrO_2 + H_2O \rightarrow IrO_2(OH) + H^+ + e^- \quad (2)$$

In which $IrO_2(OH)$ species eventually chemically decompose into IrO(OH) and O_2 [44]:

$$2\ IrO_2(OH) \rightarrow 2\ IrO(OH) + O_2 \quad (3)$$

Alternatively, based on *operando* near-ambient pressure X-ray photoelectron and absorption spectroscopy results, Pfeifer *et al*. [45, 56-57] and Saveleva *et al*. [36] proposed that the oxygen (O) anions rather than the Ir cations play a key role in the OER mechanism (O anion *red* – *ox* mechanism). These authors argue that O(-I) anions are formed via an electrochemical step. However, because of their electron-deficient nature, O(-I) anions are prone to nucleophilic attack by water molecules hence favouring the O-O bond formation through a chemical step [58-59]. Finally, other mechanisms consider both the electronic transitions of O and Ir atoms and assume that lattice O atoms participate in the OER mechanism, leading to the formation of oxygen vacancies and dissolution of Ir atoms [60-63].

In the light of our results, we assigned Reaction (1) to the Ir(III)/Ir(IV) redox couple observed at *ca*. 0.95 V *vs*. RHE, and Reaction (2) to the Ir(IV)/ Ir(V) redox peak emerging at *ca*. 1.4 - 1.45 V *vs*. RHE [30, 33, 43-44]. As shown by Kasian *et al.*[64] using differential electrochemical mass spectrometry, the fate of Ir(III) species depends on the value of the electrochemical potential: at low electrochemical potential (E < 1.6 V *vs*. RHE), Ir(III)

species are oxidized to Ir(V) whereas at high electrochemical potential, Ir(V) species are further oxidized leading ultimately to formation of gaseous IrO_3.

Besides the increase of the mean oxidation state of Ir, the O1s XPS spectra (**Figure S6**) and the O1s/Ir4f integrated intensities ratios (**Table S3**) evidence that the fraction of OH species and water molecules adsorbed on IrO_x/C and Ir/C comm. increased during the AST. In contrast, no change in the hydroxyl/water coverage was noticed on the benchmark micrometre-sized IrO_2 particles. Our findings are in line with the experimental observations of Abbott *et al.*[65] after an AST composed of 250 potential steps between 1.00 and 1.60 V *vs*. RHE. Combining the XPS results in the O1s region with the changes observed in the CVs during the AST (**Figure 5**), we thus assign the peak emerging at *ca*. 1.20 V *vs.* RHE during the AST to the oxidation of O(-II) in O(-I) (reaction (4) proposed by Pfeifer *et al.*[45]):

$$IrO_xO(-II)H \rightarrow IrO_xO(-I) + H^+ + e^- \quad (4)$$

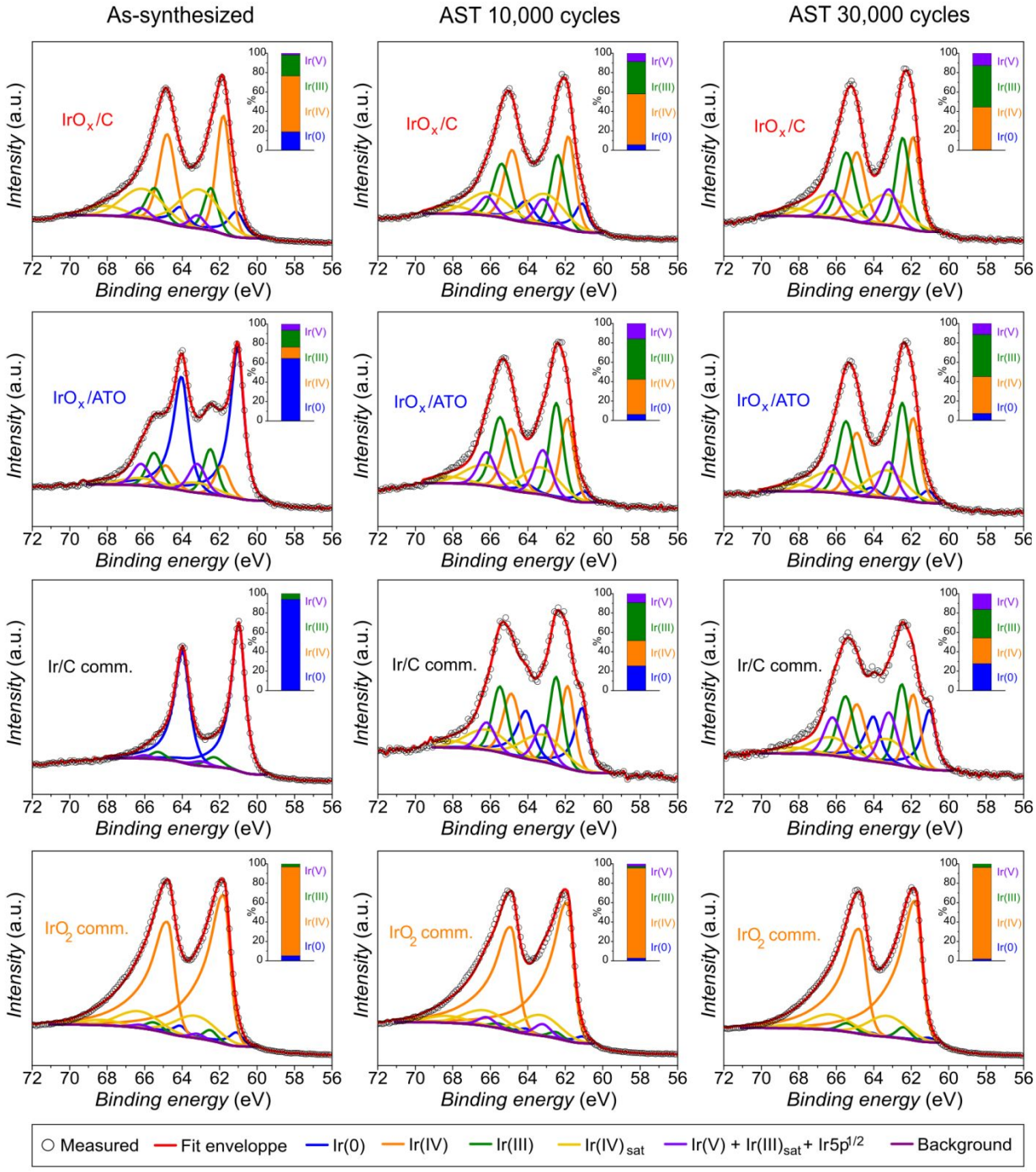
As-synthesized
AST 10,000 cycles
AST 30,000 cycles
IrOx/C
IrOx/ATO
Ir/C comm.
IrO2 comm.
Intensity (a.u.)
Binding energy (eV)
Ir(V)
Ir(III)
Ir(IV)
Ir(0)
Measured
Fit enveloppe
Ir(0)
Ir(IV)
Ir(III)
Ir(IV)sat
Ir(V) + Ir(III)sat + Ir5p1/2
Background

Figure 8. X-ray photoelectron spectra of the Ir4f level on IrO_x/C, IrO_x/ATO, Ir/C comm. and IrO_2 comm. before and after 10,000 and 30,000 potential cycles. Insets show the percentage of Ir(0), Ir(IV), Ir(III) and Ir(V). To estimate the intensity of the peak ascribed to the Ir(V) component, we subtracted 15% of the area of the peak attributed to Ir(III) and 2.67% of the total area of the Ir4f band (to account for the theoretical contribution of Ir(III) satellites and $Ir5p_{1/2}$, respectively) to the areas of the peaks located at 63.1 and 66.1 eV.

Disclosing Chemical Composition – OER Activity - Stability Relationships

To disclose chemical composition - OER activity- stability relationships, the information obtained from IL-TEM and XPS were combined. We assumed that the OER activity of the IrO_x NPs after 10 k potential cycles can be expressed as:

$$\frac{100 \text{ x } j_{meas}}{(1-\%_{lost})} = j(Ir(0)) \times \%(Ir(0)) + j(Ir(IV)) \times \%(Ir(IV)) + j(Ir(III/V)) \times \%(Ir(III) + Ir(V)) \quad (5)$$

Where j_{meas} is the background and Ohmic-drop corrected OER specific activity after 10 k potential cycles extracted from **Figure S7**, $\%_{lost}$ is the percentage of lost electrochemically active surface area between the conditioning step and the 10 k potential cycled sample estimated using IL-TEM images, $j(Ir(A))$ is the intrinsic OER specific activity of Ir in the oxidation state +A, and $\%(Ir(A))$ is the fraction of oxide in the oxidation state +A estimated from XPS spectra fits. Since the +III and +V oxidation states of Ir are related by Equation (3), their intrinsic contributions to the intrinsic OER activity were considered interdependent.

Applying Equation (5) to IrO_x/C, IrO_x/ATO, Ir/C comm. (due to the micrometre-size of the particles, IL-TEM measurements could not be performed on the IrO_2 comm. catalyst) led to a system of three equations and three unknowns, which was solved, and the calculated intrinsic OER specific activity values of Ir(0), Ir(III/V) and Ir(IV) are presented in **Table 1**. Verification of the results was achieved by comparing the measured (j_{meas}) and calculated values (j_{calc}) of the OER specific activity after the conditioning step (**Table 2**)

and the values used for the calculation and for the verification are given in **Table S4** and **Table S5**.

Table 1. Calculated intrinsic OER specific activity values of Ir(0), Ir(III/V) and Ir(IV).

	j (mA mC^{-1})	OER activity contribution (%)
j_{calc}(Ir(0))	0.0539	16.3
j_{calc}(Ir(III/V))	0.2373	71.5
j_{calc}(Ir(IV))	0.0406	12.2

Table 2. Verification of the model using the measured (j_{meas}) and calculated (j_{calc}) OER activities after the conditioning step.

	IrO_x/C	IrO_x/ATO	Ir/C comm.	IrO_2 comm.

j_{meas} (mA mC^{-1})	0.3793	0.3726	0.2660	0.03152
j_{calc} (mA mC^{-1})	0.1118	0.1700	0.1563	0.0491
Error (%)	70.5	54.4	41.2	35.8

In view of the assumptions (areas analysed in IL-TEM and XPS representative of the sample) and the uncertainties (size and shape of nanoparticles, chemical composition) associated with the different physico-chemical measurements, we first stress that the values of OER activities calculated from Equation (5) must be regarded as semi-quantitative. Despite this, some interesting findings emerge from **Table 1**. First, the results indicate that the combined Ir (III) and Ir(V) valencies are far more active for OER than Ir(0) and Ir(IV), thus confirming the better OER activity of Ir oxyhydroxides reported in the literature [30-31, 33]. This trend is independent on the OER mechanism since the Ir(III) valency plays a key role both in the Ir cation *red* - *ox* mechanism (Ir(III) – Ir(IV) – Ir(V) transitions [33, 37, 54-55, 64]) and in the O anion *red* - *ox* mechanism (the Ir(III) valency is the most likely to accommodate electrophilic O(-I) species [45]). Second, the results of the

combined IL-TEM – XPS – electrocatalytic measurements indicate that the progressive increase of the Ir(IV) fraction associated with the decrease in the number of isolated nanoparticles (due to Ir dissolution and migration/agglomeration/coalescence/detachment of the IrO_x nanoparticles) concomitantly contribute to the drop of the OER mass activity in the long-term.

CONCLUSION

In conclusion, by combining accelerated stress tests, IL-TEM and XPS measurements, we rationalized OER activity losses in simulated PEMWE anode operating conditions. IL-TEM images showed that IrO_x NPs are prone to dissolve during the conditioning stage and migrate/agglomerate/coalesce/detach in OER conditions, independently on the type of support (Vulcan XC72 and ATO). XPS analyses revealed that these morphological changes are accompanied by gradual oxidation of Ir(0) and Ir(III) into Ir(IV) and Ir(V) species along with increased concentration of hydroxyl groups and water molecules on IrO_x nanocatalysts. In contrast, no change in the mean oxidation state, no change in the

hydroxyl/water coverage and constant OER activity were noticed on the benchmark micrometre-sized IrO_2 particles. Our results thus indicate that the progressive increase of the Ir fraction with +IV valency associated with the decrease in the number of isolated nanoparticles concomitantly contribute to the drop of the specific activity towards the OER in practical PEMWE anode operating conditions.

ASSOCIATED CONTENT

Supporting Information.

The Supporting Information is available free of charge via the Internet at http://pubs.acs.org. It comprises:

- Materials and Methods

- XPS spectra (Ir4f bands) of Ir/C comm. after 10 k potential cycles.

- Changes of the Tafel slopes for all catalysts during the 10 k potential cycling protocol.

- Identical-location transmission electron microscopy of IrO_x/ATO and Ir/C comm. during the 50 k potential cycling protocol.

- Comparison of IrO_x NP size distribution achieved by automated determination or by eye-counting.

- XPS spectra (O1s band) of IrO_x/C, Ir/C comm. and IrO_2 comm., before and after 10 k and 30 k potential cycles.

- Changes of the OER catalytic activity as a function of the number of AST cycles for all catalysts.

- Parameters used to fit the XPS spectra (Ir4f and O1s band).

- Atomic percentages of the different Ir valencies for the as-synthesized catalysts.

- O1s/Ir4f integrated intensities ratios for the as-synthesized and aged (10 k or 30 k potential cycles) IrO_x/C, Ir/C comm. and IrO_2 comm. catalysts.

- Values used for the calculation of the intrinsic OER activities of the different Ir valencies obtained after 10 k potential cycles and values used to check this calculation obtained after the conditioning step.

AUTHOR INFORMATION

Corresponding Authors

* E-mail address for F.C: fabien.claudel@grenoble-inp.org

* E-mail address for F.M: frederic.maillard@lepmi.grenoble-inp.fr

Author Contributions

All authors analysed, discussed the results, drew conclusions and approved the final version of this manuscript.

CONFLICT OF INTEREST

The authors declare no competing financial interest.

ACKNOWLEDGEMENTS

This work was performed within the framework of the Centre of Excellence of Multifunctional Architectured Materials “CEMAM” n◦ ANR-10-LABX-44-01. The French National Research Agency (MOISE project, grant number ANR-17-CE05-0033) financially supported this research. F.C. acknowledges the Region Auvergne Rhônes-Alpes for funding his Ph.D. thesis in the frame of the ARC Energies program (ARC 2016 n° 04 ADR). Luis Cardenas (IRCELYON) is acknowledged for complementary XPS measurements.

REFERENCES

1. Lund, H., Renewable Energy Strategies for Sustainable Development. *Energy.* **2007,** *32*, 912-919.

2. Millet, P.; Mbemba, N.; Grigoriev, S. A.; Fateev, V. N.; Aukauloo, A.; Etiévant, C., Electrochemical Performances of PEM Water Electrolysis Cells and Perspectives. *Int. J. Hydrogen Energy.* **2011,** *36*, 4134-4142.

3. Carmo, M.; Fritz, D. L.; Mergel, J.; Stolten, D., A Comprehensive Review on PEM Water Electrolysis. *Int. J. Hydrogen Energy.* **2013,** *38*, 4901-4934.

4. Miles, M. H.; Thomason, M. A., Periodic Variations of Overvoltages for Water Electrolysis in Acid Solutions from Cyclic Voltammetric Studies. *J. Electrochem. Soc.* **1976,** *123*, 1459-1461.

5. Miles, M. H.; Klaus, E. A.; Gunn, B. P.; Locker, J. R.; Serafin, W. E.; Srinivasan, S., The Oxygen Evolution Reaction on Platinum, Iridium, Ruthenium and Their Alloys at 80°C in Acid Solutions. *Electrochim. Acta.* **1978,** *23*, 521-526.

6. Trasatti, S., Electrocatalysis in the Anodic Evolution of Oxygen and Chlorine. *Electrochim. Acta.* **1984,** *29*, 1503-1512.

7. Kötz, R.; Stucki, S., Stabilization of RuO_2 by IrO_2 for Anodic Oxygen Evolution in Acid Media. *Electrochim. Acta.* **1986,** *31*, 1311-1316.

8. Matsumoto, Y.; Sato, E., Electrocatalytic Properties of Transition Metal Oxides for Oxygen Evolution Reaction. *Mater. Chem. Phys.* **1986,** *14*, 397-426.

9. Cheng, J. B.; Zhang, H. M.; Chen, G. B.; Zhang, Y. N., Study of $Ir_xRu_{1-x}O_2$ Oxides as Anodic Electrocatalysts for Solid Polymer Electrolyte Water Electrolysis. *Electrochim. Acta.* **2009,** *54*, 6250-6256.

10. Andolfatto, F.; Durand, R.; Michas, A.; Millet, P.; Stevens, P., Solid Polymer Electrolyte Water Electrolysis: Electrocatalysis and Long-Term Stability. *Int. J. Hydrogen Energy.* **1994,** *19*, 421-427.

11. Da Silva, L. A.; Alves, V. A.; Da Silva, M. A. P.; Trasatti, S.; Boodts, J. F. C., Oxygen Evolution in Acid Solution on IrO_2 + TiO_2 Ceramic Films. A Study by Impedance, Voltammetry and SEM. *Electrochim. Acta.* **1997,** *42*, 271-281.

12. Chen, G.; Chen, X.; Yue, P. L., Electrochemical Behavior of Novel Ti/IrO_x-Sb_2O_5-SnO_2 Anodes. *J. Phys. Chem. B.* **2002,** *106*, 4364-4369.

13. Rasten, E.; Hagen, G.; Tunold, R., Electrocatalysis in Water Electrolysis with Solid Polymer Electrolyte. *Electrochim. Acta.* **2003,** *48*, 3945-3952.

14. Hu, J. M.; Zhang, J. Q.; Cao, C. N., Oxygen Evolution Reaction on IrO_2-Based DSA® Type Electrodes: Kinetics Analysis of Tafel Lines and EIS. *Int. J. Hydrogen Energy.* **2004,** *29*, 791-797.

15. Song, S.; Zhang, H.; Ma, X.; Shao, Z.; Baker, R. T.; Yi, B., Electrochemical Investigation of Electrocatalysts for the Oxygen Evolution Reaction in PEM Water Electrolyzers. *Int. J. Hydrogen Energy.* **2008,** *33*, 4955-4961.

16. Mayousse, E.; Maillard, F.; Fouda-Onana, F.; Sicardy, O.; Guillet, N., Synthesis and Characterization of Electrocatalysts for the Oxygen Evolution in PEM Water Electrolysis. *Int. J. Hydrogen Energy.* **2011,** *36*, 10474-10481.

17. Reier, T.; Pawolek, Z.; Cherevko, S.; Bruns, M.; Jones, T.; Teschner, D.; Selve, S.; Bergmann, A.; Nong, H. N.; Schlögl, R.; Mayrhofer, K. J. J.; Strasser, P., Molecular Insight in Structure and Activity of Highly Efficient, Low-Ir Ir-Ni Oxide Catalysts for Electrochemical Water Splitting (OER). *J. Am. Chem. Soc.* **2015,** *137*, 13031-13040.

18. Marshall, A.; Børresen, B.; Hagen, G.; Tsypkin, M.; Tunold, R., Electrochemical Characterisation of $Ir_xSn_{1-x}O_2$ Powders as Oxygen Evolution Electrocatalysts. *Electrochim. Acta.* **2006,** *51*, 3161-3167.

19. Di Blasi, A.; D'Urso, C.; Baglio, V.; Antonucci, V.; Arico, A. S.; Ornelas, R.; Matteucci, F.; Orozco, G.; Beltran, D.; Meas, Y.; Arriaga, L. G., Preparation and Evaluation of RuO_2-IrO_2, IrO_2-Pt and IrO_2-Ta_2O_5 Catalysts for the Oxygen Evolution Reaction in an SPE Electrolyzer. *J. Appl. Electrochem.* **2009,** *39*, 191-196.

20. Marshall, A.; Børresen, B.; Hagen, G.; Sunde, S.; Tsypkin, M.; Tunold, R., Iridium Oxide-Based Nanocrystalline Particles as Oxygen Evolution Electrocatalysts. *Russ. J. Electrochem.* **2006,** *42*, 1134-1140.

21. Cheng, J.; Zhang, H.; Ma, H.; Zhong, H.; Zou, Y., Preparation of $Ir_{0.4}Ru_{0.6}Mo_xO_y$ for Oxygen Evolution by Modified Adams' Fusion Method. *Int. J. Hydrogen Energy.* **2009,** *34*, 6609-6613.

22. Pérez-Viramontes, N. J.; Escalante-García, I. L.; Guzmán-Martínez, C.; Galván-Valencia, M.; Durón-Torres, S. M., Electrochemical Study of Ir–Sn–Sb–O Materials as

Catalyst-Supports for the Oxygen Evolution Reaction. *J. Appl. Electrochem.* **2015,** *45*, 1165-1173.

23. Reier, T.; Oezaslan, M.; Strasser, P., Electrocatalytic Oxygen Evolution Reaction (OER) on Ru, Ir, and Pt Catalysts: A Comparative Study of Nanoparticles and Bulk Materials. *ACS Catal.* **2012,** *2*, 1765-1772.

24. Oh, H. S.; Nong, H. N.; Reier, T.; Gliech, M.; Strasser, P., Oxide-Supported Ir Nanodendrites with High Activity and Durability for the Oxygen Evolution Reaction in Acid PEM Water Electrolyzers. *Chem. Sci.* **2015,** *6*, 3321-3328.

25. Kinoshita, K., *Carbon: Electrochemical and Physicochemical Properties*. John Wiley & Sons: New York, 1988.

26. Cognard, G. Electrocatalyseurs À Base d'Oxydes Métalliques Poreux Pour Pile À Combustible à Membrane Échangeuse de Protons. Université Grenoble Alpes, France, 2017.

27. Ávila-Vázquez, V.; Cruz, J. C.; Galván-Valencia, M.; Ledesma-García, J.; Arriaga, L. G.; Guzmán, C.; Durón-Torres, S. M., Electrochemical Study of Sb-Doped SnO_2 Supports on the Oxygen Evolution Reaction: Effect of Synthesis Annealing Time. *Int. J. Electrochem. Sci.* **2013,** *8*, 10586-10600.

28. Ma, L.; Sui, S.; Zhai, Y., Investigations on High Performance Proton Exchange Membrane Water Electrolyzer. *Int. J. Hydrogen Energy.* **2009,** *34*, 678-684.

29. Fuentes, R. E.; Farell, J.; Weidner, J. W., Multimetallic Electrocatalysts of Pt, Ru, and Ir Supported on Anatase and Rutile TiO_2 for Oxygen Evolution in an Acid Environment. *Electrochem. Solid-State Lett.* **2011,** *14*, E5-E7.

30. Gottesfeld, S.; Srinivasan, S., Electrochemical and Optical Studies of Thick Oxide Layers on Iridium and Their Electrocatalytic Activities for the Oxygen Evolution Reaction. *J. Electroanal. Chem. Interfacial Electrochem.* **1978,** *86*, 89-104.

31. Reier, T.; Teschner, D.; Lunkenbein, T.; Bergmann, A.; Selve, S.; Kraehnert, R.; Schlögl, R.; Strasser, P., Electrocatalytic Oxygen Evolution on Iridium Oxide: Uncovering

Catalyst-Substrate Interactions and Active Iridium Oxide Species. *J. Electrochem. Soc.* **2014,** *161*, F876-F882.

32. Danilovic, N.; Subbaraman, R.; Chang, K. C.; Chang, S. H.; Kang, Y.; Snyder, J.; Paulikas, A. P.; Strmcnik, D.; Kim, Y. T.; Myers, D.; Stamenkovic, V. R.; Markovic, N. M., Using Surface Segregation to Design Stable Ru-Ir Oxides for the Oxygen Evolution Reaction in Acidic Environments. *Angew. Chem. Int. Ed.* **2014,** *53*, 14016-14021.

33. Kötz, R.; Neff, H.; Stucki, S., Anodic Iridium Oxide Films: XPS-Studies of Oxidation State Changes and O_2-Evolution. *J. Electrochem. Soc.* **1984,** *131*, 72-77.

34. Kolotyrkin, Y. M.; Losev, V. V.; Chemodanov, A. N., Relationship between Corrosion Processes and Oxygen Evolution on Anodes Made from Noble Metals and Related Metal Oxide Anodes. *Mater. Chem. Phys.* **1988,** *19*, 1-95.

35. Elzanowska, H.; Birss, V. I., Reversible Ageing of Iridium Oxide Electrodes in Acidic Solutions. *J. Appl. Electrochem.* **1993,** *23*, 646-654.

36. Saveleva, V. A.; Wang, L.; Teschner, D.; Jones, T.; Gago, A. S.; Friedrich, K. A.; Zafeiratos, S.; Schlögl, R.; Savinova, E. R., *Operando* Evidence for a Universal Oxygen Evolution Mechanism on Thermal and Electrochemical Iridium Oxides. *J. Phys. Chem. Lett.* **2018,** *9*, 3154-3160.

37. Sanchez Casalongue, H. G.; Ng, M. L.; Kaya, S.; Friebel, D.; Ogasawara, H.; Nilsson, A., *In Situ* Observation of Surface Species on Iridium Oxide Nanoparticles During the Oxygen Evolution Reaction. *Angew. Chem.* **2014,** *53*, 7169-72.

38. Cognard, G.; Ozouf, G.; Beauger, C.; Berthomé, G.; Riassetto, D.; Dubau, L.; Chattot, R.; Chatenet, M.; Maillard, F., Benefits and Limitations of Pt Nanoparticles Supported on Highly Porous Antimony-Doped Tin Dioxide Aerogel as Alternative Cathode Material for Proton-Exchange Membrane Fuel Cells. *Appl. Catal. B.* **2017,** *201*, 381-390.

39. Freakley, S. J.; Ruiz-Esquius, J.; Morgan, D. J., The X-Ray Photoelectron Spectra of Ir, IrO_2 and $IrCl_3$ Revisited. *Surf. Interface Anal.* **2017,** *49*, 794-799.

40. Cherevko, S.; Geiger, S.; Kasian, O.; Kulyk, N.; Grote, J.-P.; Savan, A.; Shrestha, B. R.; Merzlikin, S.; Breitbach, B.; Ludwig, A.; Mayrhofer, K. J. J., Oxygen and Hydrogen

Evolution Reactions on Ru, RuO_2, Ir, and IrO_2 Thin Film Electrodes in Acidic and Alkaline Electrolytes: A Comparative Study on Activity and Stability. *Catal. Today.* **2016,** *262*, 170-180.

41. Lettenmeier, P.; Majchel, J.; Wang, L.; Saveleva, V. A.; Zafeiratos, S.; Savinova, E. R.; Gallet, J. J.; Bournel, F.; Gago, A. S.; Friedrich, K. A., Highly Active Nano-Sized Iridium Catalysts: Synthesis and *Operando* Spectroscopy in a Proton Exchange Membrane Electrolyzer. *Chem. Sci.* **2018,** *9*, 3570-3579.

42. Ardizzone, S.; Fregonara, G.; Trasatti, S., "Inner" and "Outer" Active Surface of RuO_2 Electrodes. *Electrochim. Acta.* **1990,** *35*, 263-267.

43. Cherevko, S.; Geiger, S.; Kasian, O.; Mingers, A.; Mayrhofer, K. J. J., Oxygen Evolution Activity and Stability of Iridium in Acidic Media. Part 1. – Metallic Iridium. *J. Electroanal. Chem.* **2016,** *773*, 69-78.

44. Cherevko, S.; Geiger, S.; Kasian, O.; Mingers, A.; Mayrhofer, K. J. J., Oxygen Evolution Activity and Stability of Iridium in Acidic Media. Part 2. – Electrochemically Grown Hydrous Iridium Oxide. *J. Electroanal. Chem.* **2016,** *774*, 102-110.

45. Pfeifer, V.; Jones, T. E.; Velasco Velez, J. J.; Arrigo, R.; Piccinin, S.; Havecker, M.; Knop-Gericke, A.; Schlögl, R., *In Situ* Observation of Reactive Oxygen Species Forming on Oxygen-Evolving Iridium Surfaces. *Chem. Sci.* **2017,** *8*, 2143-2149.

46. Schlögl, K.; Mayrhofer, K. J. J.; Hanzlik, M.; Arenz, M., Identical-Location TEM Investigations of Pt/C Electrocatalyst Degradation at Elevated Temperatures. *J. Electroanal. Chem.* **2011,** *662*, 355-360.

47. Cherevko, S.; Zeradjanin, A. R.; Topalov, A. A.; Kulyk, N.; Katsounaros, I.; Mayrhofer, K. J. J., Dissolution of Noble Metals During Oxygen Evolution in Acidic Media. *ChemCatChem.* **2014,** *6*, 2219-2223.

48. Cherevko, S.; Reier, T.; Zeradjanin, A. R.; Pawolek, Z.; Strasser, P.; Mayrhofer, K. J. J., Stability of Nanostructured Iridium Oxide Electrocatalysts During Oxygen Evolution Reaction in Acidic Environment. *Electrochem. Com.* **2014,** *48*, 81-85.

49. Pourbaix, M., *Atlas of Electrochemical Equilibria in Aqueous Solutions*. Pergamon: 1966; Vol. 1.

50. Castanheira, L.; Silva, W. O.; Lima, F. H. B.; Crisci, A.; Dubau, L.; Maillard, F., Carbon Corrosion in Proton-Exchange Membrane Fuel Cells: Effect of the Carbon Structure, the Degradation Protocol, and the Gas Atmosphere. *ACS Catal.* **2015,** *5*, 2184-2194.

51. Durst, J.; Lamibrac, A.; Charlot, F.; Dillet, J.; Castanheira, L. F.; Maranzana, G.; Dubau, L.; Maillard, F.; Chatenet, M.; Lottin, O., Degradation Heterogeneities Induced by Repetitive Start/Stop Events in Proton Exchange Membrane Fuel Cell: Inlet *vs*. Outlet and Channel *vs*. Land. *Appl. Catal. B.* **2013,** *138-139*, 416-426.

52. Cognard, G.; Ozouf, G.; Beauger, C.; Dubau, L.; López-Haro, M.; Chatenet, M.; Maillard, F., Insights into the Stability of Pt Nanoparticles Supported on Antimony-Doped Tin Oxide in Different Potential Ranges. *Electrochim. Acta.* **2017,** *245*, 993-1004.

53. Li, T.; Kasian, O.; Cherevko, S.; Zhang, S.; Geiger, S.; Scheu, C.; Felfer, P.; Raabe, D.; Gault, B.; Mayrhofer, K. J. J., Atomic-Scale Insights into Surface Species of Electrocatalysts in Three Dimensions. *Nature Catal.*. **2018,** *1*, 300-305.

54. Minguzzi, A.; Lugaresi, O.; Achilli, E.; Locatelli, C.; Vertova, A.; Ghigna, P.; Rondinini, S., Observing the Oxidation State Turnover in Heterogeneous Iridium-Based Water Oxidation Catalysts. *Chem. Sci.* **2014,** *5*, 3591-3597.

55. Minguzzi, A.; Locatelli, C.; Lugaresi, O.; Achilli, E.; Cappelletti, G.; Scavini, M.; Coduri, M.; Masala, P.; Sacchi, B.; Vertova, A.; Ghigna, P.; Rondinini, S., Easy Accommodation of Different Oxidation States in Iridium Oxide Nanoparticles with Different Hydration Degree as Water Oxidation Electrocatalysts. *ACS Catal.* **2015,** *5*, 5104-5115.

56. Pfeifer, V.; Jones, T. E.; Velasco Velez, J. J.; Massue, C.; Greiner, M. T.; Arrigo, R.; Teschner, D.; Girgsdies, F.; Scherzer, M.; Allan, J.; Hashagen, M.; Weinberg, G.; Piccinin, S.; Havecker, M.; Knop-Gericke, A.; Schlögl, R., The Electronic Structure of Iridium Oxide Electrodes Active in Water Splitting. *Phys. Chem. Chem. Phys.* **2016,** *18*, 2292-6.

57. Pfeifer, V.; Jones, T. E.; Wrabetz, S.; Massue, C.; Velasco Velez, J. J.; Arrigo, R.; Scherzer, M.; Piccinin, S.; Havecker, M.; Knop-Gericke, A.; Schlogl, R., Reactive Oxygen Species in Iridium-Based OER Catalysts. *Chem Sci.* **2016,** *7*, 6791-6795.

58. Rossmeisl, J.; Logadottir, A.; Nørskov, J. K., Electrolysis of Water on (Oxidized) Metal Surfaces. *Chem. Phys.* **2005,** *319*, 178-184.

59. Rossmeisl, J.; Qu, Z. W.; Zhu, H.; Kroes, G. J.; Nørskov, J. K., Electrolysis of Water on Oxide Surfaces. *J. Electroanal. Chem.* **2007,** *607*, 83-89.

60. Fierro, S.; Nagel, T.; Baltruschat, H.; Comninellis, C., Investigation of the Oxygen Evolution Reaction on Ti/IrO_2 Electrodes Using Isotope Labelling and on-Line Mass Spectrometry. *Electrochem. Com.* **2007,** *9*, 1969-1974.

61. Geiger, S.; Kasian, O.; Ledendecker, M.; Pizzutilo, E.; Mingers, A. M.; Fu, W. T.; Diaz-Morales, O.; Li, Z.; Oellers, T.; Fruchter, L.; Ludwig, A.; Mayrhofer, K. J. J.; Koper, M. T. M.; Cherevko, S., The Stability Number as a Metric for Electrocatalyst Stability Benchmarking. *Nature Catal.* **2018,** *1*, 508-515.

62. Grimaud, A.; Demortière, A.; Saubanère, M.; Dachraoui, W.; Duchamp, M.; Doublet, M.-L.; Tarascon, J.-M., Activation of Surface Oxygen Sites on an Iridium-Based Model Catalyst for the Oxygen Evolution Reaction. *Nature Energy.* **2016,** *2*, 16189.

63. Grimaud, A.; Diaz-Morales, O.; Han, B.; Hong, W. T.; Lee, Y. L.; Giordano, L.; Stoerzinger, K. A.; Koper, M. T. M.; Shao-Horn, Y., Activating Lattice Oxygen Redox Reactions in Metal Oxides to Catalyse Oxygen Evolution. *Nat. Chem.* **2017,** *9*, 457-465.

64. Kasian, O.; Grote, J. P.; Geiger, S.; Cherevko, S.; Mayrhofer, K. J. J., The Common Intermediates of Oxygen Evolution and Dissolution Reactions During Water Electrolysis on Iridium. *Angew. Chem., Int. Ed. Engl.* **2018,** *57*, 2488-2491.

65. Abbott, D. F.; Lebedev, D.; Waltar, K.; Povia, M.; Nachtegaal, M.; Fabbri, E.; Copéret, C.; Schmidt, T. J., Iridium Oxide for the Oxygen Evolution Reaction: Correlation between Particle Size, Morphology, and the Surface Hydroxo Layer from *Operando* XAS. *Chem. Mater.* **2016,** *28*, 6591-6604.

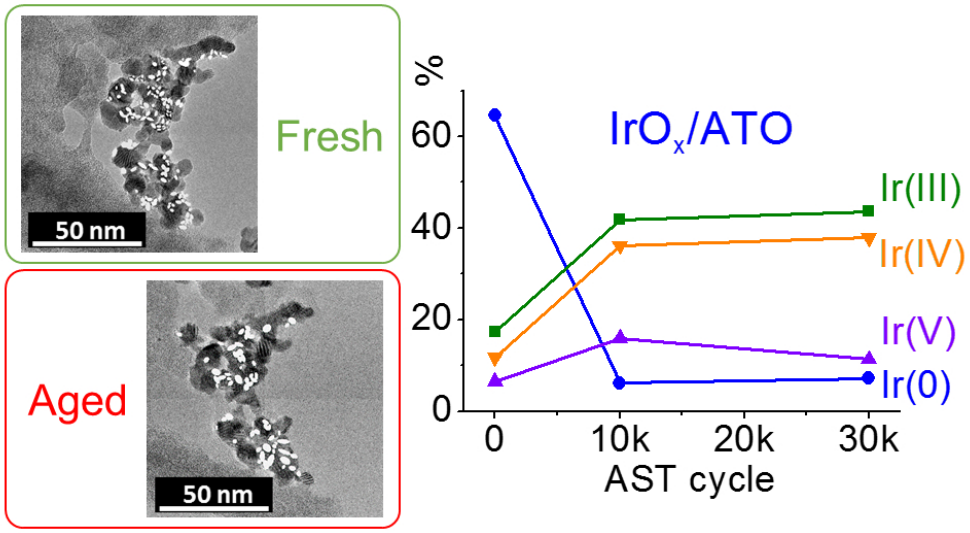

Identical-location transmission electron microscopy, X-ray photoelectron spectroscopy and electrochemistry were combined to unravel the degradation mechanisms of iridium oxide nanoparticles in oxygen evolution reaction conditions.

82x44mm (300 x 300 DPI)